ADVANCES IN ATMOSPHERIC SCIENCES, VOL. 37, JANUARY 2020, 18–28

• Data Description Article •

CAS FGOALS-f3-L Model Datasets for CMIP6 GMMIP Tier-1 and Tier-3 Experiments

Bian HE[1,2,3], Yimin LIU[*1,2,3], Guoxiong WU[1,2,3], Qing BAO[1,2,3], Tianjun ZHOU[1,2,3], Xiaofei WU[4], Lei WANG[1,3], Jiandong LI[1,3], Xiaocong WANG[1,2,3], Jinxiao LI[1,3], Wenting HU[1,3], Xiaoqi ZHANG[5,1], Chen SHENG[1,3], and Yiqiong TANG[5,1]

[1]*State Key Laboratory of Numerical Modeling for Atmospheric Sciences and Geophysical Fluid Dynamics, Institute of Atmospheric Physics, Chinese Academy of Sciences, Beijing* 100029, *China*

[2]*Chinese Academy of Sciences Center for Excellence in Tibetan Plateau Earth Sciences, Beijing* 100101, *China*

[3]*College of Earth and Planetary Sciences, University of Chinese Academy of Sciences, Beijing* 100029, *China*

[4]*School of Atmospheric Sciences/Plateau Atmosphere and Environment Key Laboratory of Sichuan Province, Chengdu University of Information Technology, Chengdu, Sichuan* 610225, *China*

[5]*Nanjing University of Information Science and Technology, Nanjing, Jiangsu* 210044, *China*

(Received 18 April 2019; revised 12 July 2019; accepted 22 August 2019)

ABSTRACT

The Chinese Academy of Sciences (CAS) Flexible Global Ocean–Atmosphere–Land System (FGOALS-f3-L) model datasets prepared for the sixth phase of the Coupled Model Intercomparison Project (CMIP6) Global Monsoons Model Intercomparison Project (GMMIP) Tier-1 and Tier-3 experiments are introduced in this paper, and the model descriptions, experimental design and model outputs are demonstrated. There are three simulations in Tier-1, with different initial states, and five simulations in Tier-3, with different topographies or surface thermal status. Specifically, Tier-3 contains four orographic perturbation experiments that remove the Tibetan–Iranian Plateau, East African and Arabian Peninsula highlands, Sierra Madre, and Andes, and one thermal perturbation experiment that removes the surface sensible heating over the Tibetan–Iranian Plateau and surrounding regions at altitudes above 500 m. These datasets will contribute to CMIP6's value as a benchmark to evaluate the importance of long-term and short-term trends of the sea surface temperature in monsoon circulations and precipitation, and to a better understanding of the orographic impact on the global monsoon system over highlands.

Key words: global monsoon, CMIP6, GMMIP, Tibetan Plateau, orographic perturbation

Citation: He, B., and Coauthors, 2020: CAS FGOALS-f3-L model datasets for CMIP6 GMMIP Tier-1 and Tier-3 experiments. *Adv. Atmos. Sci.*, **37**(1), 18–28, https://doi.org/10.1007/s00376-019-9085-y.

Article Highlights:

- GMMIP Tier-1 simulation datasets produced by CAS FGOALS-f3-L which covering 1870 to 2014 with three ensemble members.
- GMMIP Tier-3 simulations contain five orographically perturbation experiments.
- The model outputs for Tibetan Plateau perturbation experiments include 6-hourly and 3 hourly datasets.

1. Introduction

The prediction of changes in global monsoon rainfall and associated atmospheric circulation is of great societal concern and scientific importance. The global monsoon system can basically be divided into several submonsoon systems, including the Asian, Australian, northern and southern African, North American and South American monsoons (Wang, 1994; Wang and Ding, 2008). Each monsoon system has its own unique temporal and spatial features. The accurate predictions of these monsoon behaviors are still a challenge for current climate models (Wang et al., 2005; Zhou et al., 2009a; Cook et al., 2012; Kitoh et al., 2013; Sperber et al., 2013; Song and Zhou, 2014a, b). These challenges arise from our insufficient understanding of the complex atmosphere–ocean–land interactions involved in the monsoon systems that are driven by external forcing and internal variabilities

* Corresponding author: Yimin LIU
Email: lym@lasg.iap.ac.cn

(Folland et al., 1986; Power et al., 1999; Enfield et al., 2001; Mantua and Hare, 2002; Sutton and Hodson, 2005; Goswami et al., 2006; Lu et al., 2006; Zhou et al., 2009b; Wang et al., 2012).

Global highlands have great influence on global monsoons. Previous studies suggest that highlands, especially the Tibetan–Iranian Plateau (TIP) highlands over the Asian continent, could exert both mechanical and thermal forcings on the surrounding atmosphere and lead to changes in the global monsoon system and hydrological cycle (Queney, 1948; Hahn and Manabe, 1975; Kitoh, 1997; Abe et al., 2003; Liu et al., 2007; Okajima and Xie, 2007; Wu et al., 2007; Zhou et al., 2009c). However, debate still exists on how the TIP modulates the Asian monsoon system (Boos and Kuang, 2010, 2013; Wu et al., 2012; He et al., 2015; Wu et al., 2015). The different understandings of the effect of the TIP climate originate from both the lack of observation datasets and limitations to the simulation ability of climate models.

The Global Monsoons Model Intercomparison Project (GMMIP) is one of the endorsed MIPs in the sixth phase of the Coupled Model Intercomparison Project (CMIP6). It designed a series of extended Tier-1 Atmospheric Model Intercomparison Project (AMIP) experiments to understand the behavior of monsoon circulations and associated precipitation over the late 19th through the early 21st centuries. It also designed Tier-3 orographic perturbation experiments to quantitatively understand the regional response to orographic perturbation from both thermal and dynamic aspects (Zhou et al., 2016). In addition to the TIP orography, the Tier-3 experiments also included orographic perturbation experiments, including experiments over the East African highlands, North American highlands, and South American highlands.

The Chinese Academy of Sciences (CAS) Flexible Global Ocean–Atmosphere–Land System (FGOALS-f3-L) climate system model, which was developed at the Institute of Atmospheric Physics (IAP)/State Key Laboratory of Numerical Modeling for Atmospheric Sciences and Geophysical Fluid Dynamics (LASG) (Zhou et al., 2012, 2015; Bao et al., 2019), recently finished GMMIP Tier-1 and Tier-3 simulations. To provide an essential model configuration and experimental method for a variety of users, we provide detailed descriptions of the model design and data outputs of the GMMIP Tier-1 and Tier-3 experiments by the CAS FGOALS-f3-L model in this study. Section 2 presents the model description and experimental design. Section 3 shows the technical validation of the FGOALS-f3-L experiments. Section 4 provides usage notes.

2. Model and experiments

2.1. *Model introduction*

The configuration of the CMIP6 version of the CAS FGOALS-f3-L model is introduced in the description paper of the AMIP datasets (He et al., 2019). For convenience for those using only the GMMIP datasets, we briefly reintroduce the model here. The CAS FGOALS-f3-L model is structured with five components: version 2.2 of the Finite-volume Atmospheric model (FAMIL) (Zhou et al., 2015; Bao et al., 2019; Li et al., 2019), which is the next generation atmospheric general circulation model (AGCM) Spectral Atmospheric Model (SAMIL) (Wu et al., 1996; Bao et al., 2010, 2013); version 3 of the LASG/IAP Climate system Ocean Model (LICOM3) (Liu et al., 2012); version 4.0 of the Community Land Model (CLM4) (Oleson et al., 2010); and version 4 of the Los Alamos sea ice model (CICE4) (Hunke et al., 2010). The fluxes are exchanged between these components using version 7 of the coupler module from the National Center for Atmospheric Research (NCAR) (http://www.cesm.ucar.edu/models/cesm1.0/cpl7/).

The atmospheric component of FAMIL adopts a three-dimensional finite-volume dynamical core (Lin, 2004) over cubed-sphere grids (Putman and Lin, 2007) with six tiles over the globe. In the CAS FGOALS-f3-L model, each tile contains 96 grids (C96). For the globe, the longitudinal extent is divided into 384 grids, and the latitudinal area is divided into 192 grids, which results in an approximate 1° horizontal resolution. In the vertical direction, the model adopts hybrid coordinates with 32 layers, where the model top is 2.16 hPa. The main physical packages include a new moisture turbulence parameterization scheme for the boundary layer (Bretherton and Park, 2009), with shallow convection updated (Wang and Zhang, 2014). The GFDL (Geophysical Fluid Dynamics Laboratory) version of the single-moment six-category cloud microphysics scheme (Lin et al., 1983, Harris and Lin, 2014) is adopted to predict the bulk contents of water vapor, cloud water, cloud ice, rain, snow and graupel. For the cloud fraction diagnosis, the Xu and Randall (1996) scheme is used, which considers not only relative humidity but also the cloud mixing ratio, thus providing a more precise cloud fraction. A resolved convective precipitation parameterization (©2017 FAMIL Development Team) is used where, in contrast to conventional convective parameterization, convective and stratiform precipitation are calculated explicitly. In addition, a gravity wave drag scheme is also considered (Palmer et al., 1986).

2.2. *Experiments*

For the GMMIP Tier-1 experiments, three AMIP-type experiments are conducted, as summarized in Table 1. In these experiments, external forcings are prescribed as their monthly mean observation values, as recommended by previous CMIP6 projects: historical greenhouse gas concentrations from Meinshausen et al. (2017); solar forcing from Matthes et al. (2017); historical ozone concentrations from http://blogs.reading.ac.uk/ccmi/forcing-databases-in-support-of-cmip6/; and AMIP SST and sea ice datasets from PCMDI (the Program for Climate Model Diagnosis & Intercomparison) at https://esgf-node.llnl.gov/projects/esgf-llnl/. The aerosol mass concentrations are also defined and taken from CAM-Chem (the NCAR Community Atmospheric Model with Chemistry) (Lamarque et al., 2012), including

Table 1. Experimental design.

	Experiment_id	Variant_label	Integration time	Experimental design
Tier-1	amip-hist	r1i1p1f1	1861–2014	The model integration starts from 1 January 1861 with the external forcings, including greenhouse gases, solar irradiance, ozone, aerosols, SSTs and sea ice, as defined by the observed values. The first nine integration years are recognized as the spin-up time, and the outputs from 1870 to 2014 are provided for analysis.
	amip-hist	r2i1p1f1	1862–2014	Same as r1i1p1f1, but the first eight integration years are recognized as the spin-up time, and the outputs from 1870 to 2014 are provided for analysis.
	amip-hist	r3i1p1f1	1863–2014	Same as r1i1p1f1, but the first seven integration years are recognized as the spin-up time, and the outputs from 1870 to 2014 are provided for analysis.
Tier-3	amip-TIP	r1i1p1f1	1970–2014	The topography above 500 m is set to 500 m in a polygon region. The coordinates of the polygon corners are as follows: longitude coordinates (from west to east) are 25°E, 40°E, 50°E, 70°E, 90°E and 180°E; latitude coordinates (from south to north) are 5°N, 15°N, 20°N, 25°N, 35°N, 45°N and 75°N. The model integration starts on 1 January 1970, which is the same as that in the amip r1i1p1f1 experiment. The outputs from 1979 to 2014 are provided for analysis.
	amip-TIP-nosh	r1i1p1f1	1970–2014	Sensible heating is removed from topographies above 500 m, as in the same polygon region in amip-TIP. One practical method is to set the vertical temperature diffusion term to zero in the atmospheric thermodynamic equation at the bottom boundary layer. The model integration is the same as above.
	amip-hld	r1i1p1f1	1970–2014	Topographies of the East African Highlands in Africa and the Arabian Peninsula are modified by setting surface elevations to a certain height (500 m) in separate experiments. The East African highlands are in a polygon region. The coordinates of the polygon are as follows: longitude coordinates (from west to east) are 27°E and 52°E; latitude coordinates (from south to north) are 17°S, 20°N and 25°N, 35°N. The model integration is the same as above.
	amip-hld	r1i1p1f2	1970–2014	The topography of the Sierra Madre in North America is modified by setting surface elevations to a certain height (500 m) in separate experiments. The Sierra Madre domain is (15°–30°N, 120° –90°W). The model integration is the same as above.
	amip-hld	r1i1p1f3	1970–2014	The topography of the Andes in South America is modified by setting surface elevations to a certain height (500 m) in separate experiments. The Andes domain is (40°S–10°N, 90°–60°W). The model integration is the same as above.

sulfates, sea salts, black carbon, organic carbon, dust, and volcanos. The land-use datasets are defined by their climate mean values (Hurtt et al., 2009).

In the first "amip-hist" experiment, "r1i1p1f1", model integration starts from 1 January 1861 with the defined observations. The first nine integration years are recognized as the spin-up time, and the outputs from 1870 to 2014 are provided for analysis. The next two simulations, "r2i1p1f1" and "r3i1p1f1", are the same as "r1i1p1f1" but with different initial times.

Following the design of the GMMIP Tier-3 experiments (Zhou et al., 2016), five AMIP-type experiments are conducted, as summarized in Table 1. All experiments are integrated from 1970 to 2014, where the first nine years are considered as the spin-up time, and the results from 1979 to 2014 are provided for analysis. These experimental settings are the same as those for the AMIP r1i1p1f1 experiment in DECK (the Diagnostic, Evaluation and Characterization of Klima), as documented in He et al. (2019).

The specific differences among the Tier-3 experiments are summarized as follows: In the first experiment (amip-TIP), the topography above 500 m is set to 500 m in the TIP region during integration. The specific coordinates of the polygon corners are also shown in Table 1. Moreover, the land use and other land surface properties remain unchanged in the land model. In the second experiment (amip-TIP-nosh), the model topography is defined by the original values, but the TIP surface is not allowed to heat the atmosphere. That is, in the boundary layer scheme, the vertical diffusion heating term is set to zero within the same polygon region where the topography is above 500 m, as it is in amip-TIP. In the third experiment (amip-hld r1i1p1f1), the topographies of the East African Highlands in Africa and the Arabian Peninsula, Sierra Madre in North America, and Andes in South America are modified by setting the surface elevations to a certain height (500 m). The coordinates of the polygon region are shown in Table 1. In the fourth (r1i1p1f2) and fifth (r1i1p1f3) experiments, the topography of the Sierra Madres in North America and the Andes in South America is modified by setting the surface elevation to a certain

height (500 m), respectively.

3. Technical validation

The Goddard Institute for Space Studies (GISS) Surface Temperature Analysis dataset (Hansen et al., 2010) is used here to justify surface air temperature (SAT) simulations in the three amip-hist experiments. This dataset is on a 2° × 2° grid and covers the period from 1880 to the present day with monthly mean anomalies. Meanwhile, the observed precipitation datasets (Becker et al., 2013) provided by the Global Precipitation Climatology Center (GPCC) are also used to verify the long-term precipitation simulations over landmasses. Here, we show the observed and simulated time series of the global land annual mean SAT anomalies and precipitation anomalies in Figs. 1a and b, respectively. The ensemble mean of the three amip-hist simulations is denoted by thick black lines, which show clear decadal variability similar to the observations (red lines). The climate warming trend is also reasonably reproduced. For the precipitation anomaly (Fig. 1b), the observed global land precipitation (red line) shows strong interannual variability, with clear decadal variations with increasing trends during 1900–55 and 1990–2014 and decreasing trends during 1956–89. These features have also been well captured by the CAS FGOALS-f3-L model with the ensemble mean outputs (thick black line). For the validation of the spatial pattern, we show the observed SAT linear trends from 1901 to 2014 in Fig. 2a. It is clear that the warming trends dominate the global pattern, despite some cooling trends in local regions. The warming trends mainly exceed 2°C over Eurasia in the midlatitudes, North America in the high latitudes, North Africa, the middle of Australia, and the north part of South America. The CAS FGOALS-f3-L model basically reproduces the global warming pattern (Fig. 2b), but the strong warming trends simulate more north than the observation in Eurasia, and the warming trends in the Southern Hemisphere are underestimated. The observed precipitation trends during 1901 to 2014 (Fig. 3a) show increasing trends, mainly over northern Eurasia, North America, and South America, and decreasing trends over the central Tibetan Plateau (TP) and North Africa. The CAS FGOALS-f3-L model basically reproduces the pattern in the Northern Hemisphere (Fig. 3b), but the intensity of the increasing trend is too weak, and the model fails to reproduce the observed pattern over South America and the decreasing trend over Africa. Overall, the model is able to capture the long-term historical global mean surface climate for both SAT and precipitation, but it fails to reproduce some regional features, especially for the precipitation trends.

Validation of the orographic perturbation experiments is also justified in this section. To check whether we have correctly carried out the sensitivity experiments, we show all five orographic forcings from the model outputs in Fig. 4. In the thermal perturbation experiment (amip-TIP-nosh), the

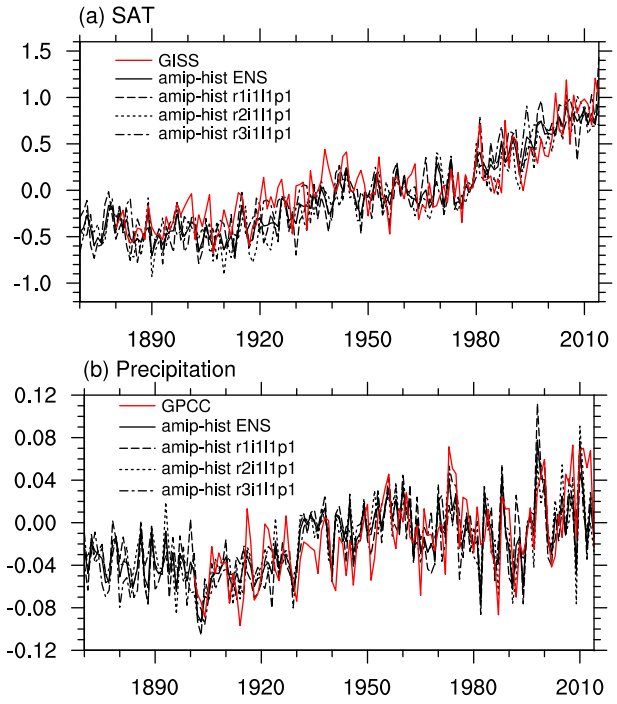

Fig. 1. (a) Time series of the global mean land SAT anomalies (units: K; relative to the mean values over 1951–1980). The red line denotes GISS datasets. The thick black line denotes the ensemble mean of the three amip-hist simulations, and the three kinds of dashed lines represent the three ensemble members: r1i1p1f1, r2i1p1f1, and r3i1p1f1. (b) As in (a) but for precipitation (units: mm d^{-1}). The red line denotes the GPCC datasets.

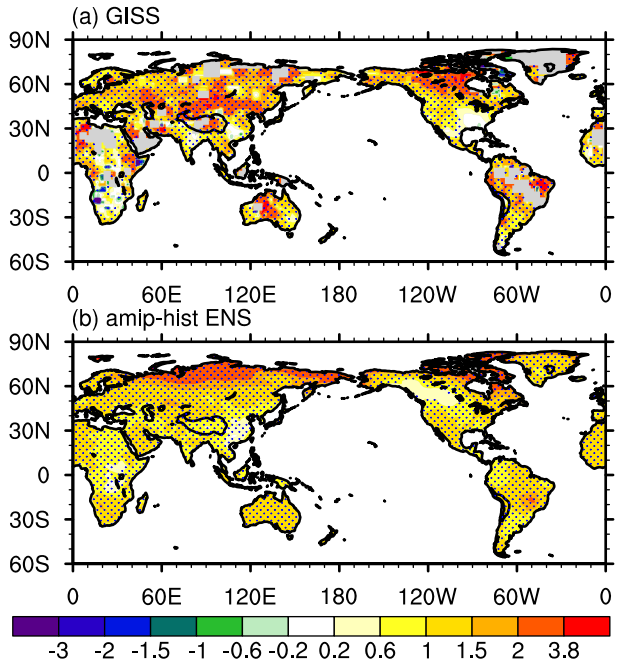

Fig. 2. Linear trends (1901–2014) of the global mean land SAT anomalies [units: K (115 $yr)^{-1}$]: (a) GISS datasets; (b) ensemble mean of the three amip-hist simulations. The blue dots denote the values that have passed the 95% significance *t*-test. The black contour denotes the 3000-m topographic height.

topography in the model is unchanged; therefore, the topography height is realistic (Fig. 4b) and similar to that in Fig. 5 in Zhou et al. (2016), which was produced by HadGEM3 (the Met Office Hadley Centre Global Environmental Model, version 3). In the amip-TIP run (Fig. 4a), the TIP region, where the topography height is above 500 m, is correctly set to 500 m following the experimental design in Table. 1. Similarly, in amip-hld r1i1p1f1 (Fig. 4c), the polygon region in

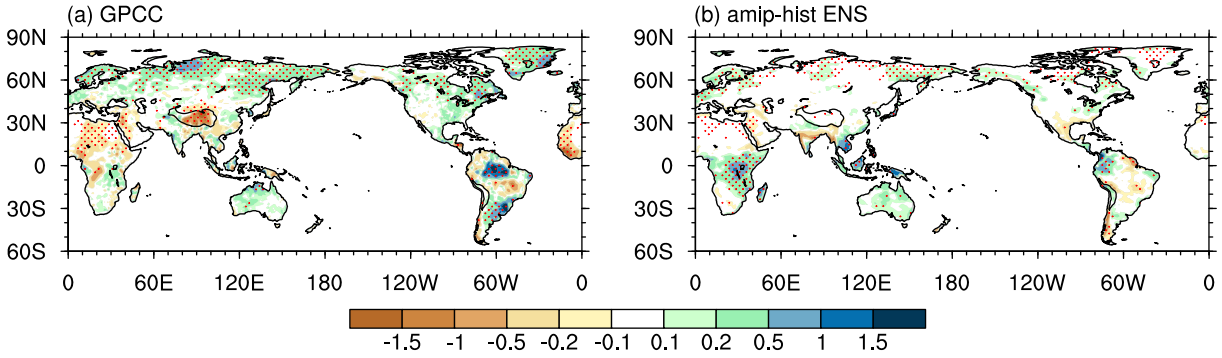

Fig. 3. Linear trends (1901–2014) of the global mean land precipitation anomalies [units: mm d^{-1} (115 $yr)^{-1}$]: (a) GPCC datasets; (b) ensemble mean of the three amip-hist simulations. The red dots denote the values that have passed the 95% significance *t*-test. The black contour denotes the 3000-m topographic height.

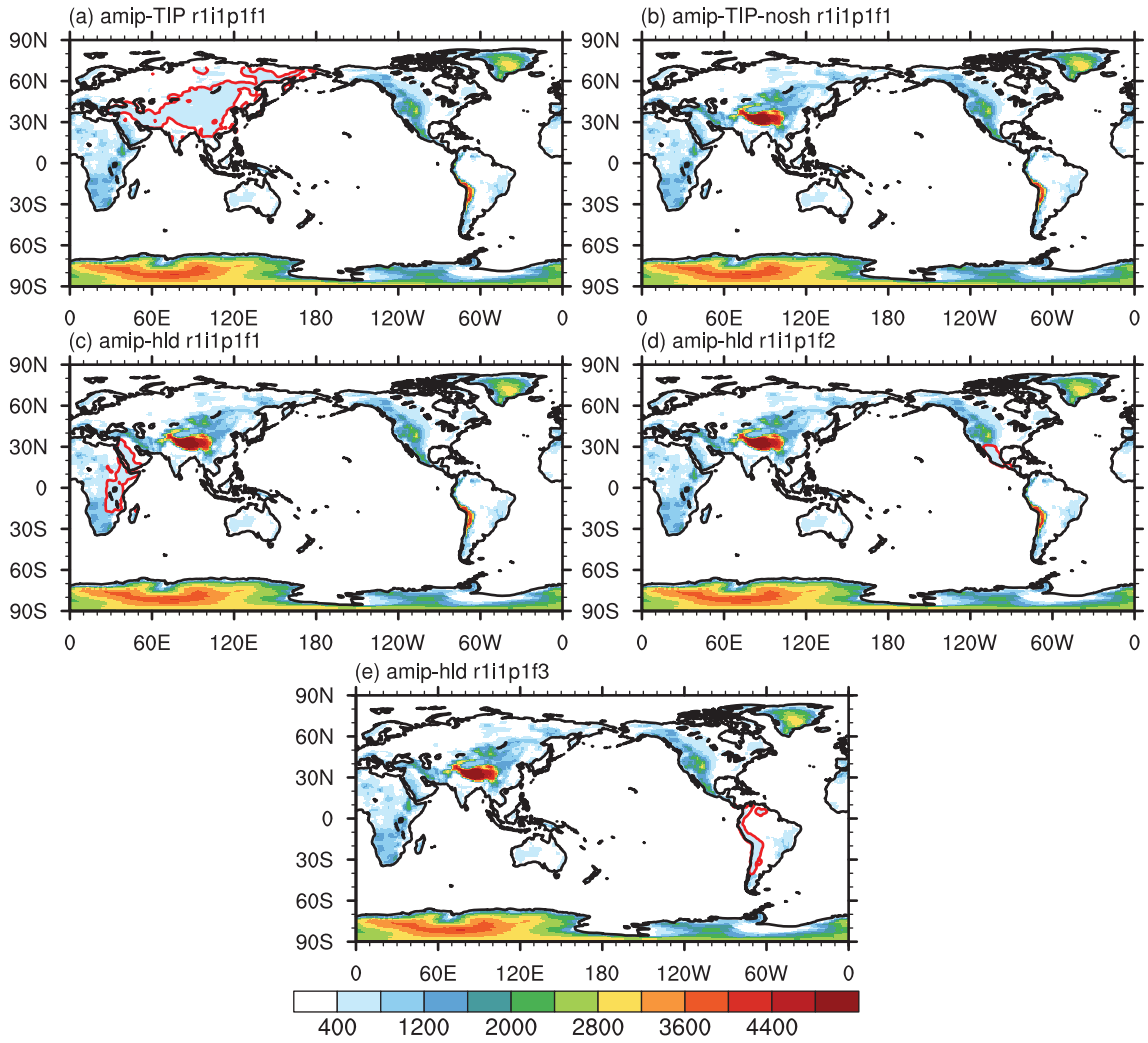

Fig. 4. Topography heights (shaded; units: m) in the experiments of (a) no TIP topography experiment amip-TIP, (b) no TIP sensible heating experiment amip-TIP-nosh, (c) no East African Highlands in Africa and the Arabian Peninsula experiment amip-hld r1i1p1f1, (d) no Sierra Madre experiment amip-hld r1i1p1f2, and (e) no Andes experiment amip-hld r1i1p1f3. The red contours denotes the modified topography.

East Africa and the Arabian Peninsula is set to 500 m; in amip-hld r1i1p1f2 (Fig. 4d), the Sierra Madre is set to 500 m; in amip-hld r1i1p1f3 (Fig. 4d), the Andes is set to 500 m. These orographic perturbations exactly follow the GMMIP Tier-3 design [Fig. 5 in Zhou et al. (2016)]. In the thermal perturbation experiment (amip-TIP-nosh), the vertical diffusion heating is set to zero throughout the integration above 500 m. We show the climatological mean (1979–2014) vertical diffusion heating of amip-TIP-nosh in Fig. 5. It is clear that in the TIP region, which is contoured by the thick black line (500 m in Fig. 5), the vertical diffusion heating is zero, which suggests that our sensitivity experiments have been carried out correctly.

4. Usage notes

As shown in section 2.1, the original model grid is C96, which has six tiles and is irregular in the horizontal direction. We merge and interpolate the tiles to a regular 1° on a global scale by first-order conservation interpolation for the nominal resolution, as required by CMIP6 for public use. The dataset format is NETCDF-4, which can be easy to read and write by software such as Climate Data Operators (https://www.unidata.ucar.edu/software/netcdf/workshops/2012/third_party/CDO.html), netCDF Operator (http://nco.sourceforge.net), NCAR Command Language (http://www.ncl.ucar.edu), and Python (https://www.python.org).

To understand the possible influence of TIP thermal and mechanical forcings on extreme events and its use in downscaling studies, potential uses may need to compare these experiments to the reference run. We recommend the CMIP6 DECK AMIP r1i1p1f1 experiment by using the CAS FGOALS-f3-L model as the reference run since these experiments share the same model and have a consistent integration method and initial state (He et al., 2019). Here, we show the climate mean responses of the TIP thermal and dynamical effect on the Asian summer monsoon in Fig. 6. The difference of the June–July–August (JJA) precipitation and 850-hPa wind between amip r1i1p1f1 and amip-TIP-nosh r1i1p1f1 (Fig. 6a) shows a similar large-scale pattern as in previous studies (Fig. 3c in Wu et al., 2012), with positive precipitation anomalies over South Asia and the North Indian Ocean and negative precipitation anomalies over the tropical Indian Ocean accompanied by cyclonic circulation around the TP. The difference between amip r1i1p1f1 and amip-TIP r1i1p1f1 (Fig. 6b) also shows similar patterns as in Fig. 2a of Wu et al. (2012), which indicates that the previous conclusions that TP heating could induce a low-level cyclonic circulation anomaly are robust to a different climate model. In addition, there also exist regional differences between the current model results (Fig. 6) and previous model results (Wu et al., 2012). For example, the positive precipitation anomalies over the western Pacific extend to the middle Pacific in the current model (Fig. 6a) but are limited to over the western North Pacific in the previous model [Fig. 3c in Wu et al. (2012)]. The reduction of this type of uncertainty requires multimodel results from GMMIP Tier-3 experiments.

The weather and climate change of the West Indian Ocean is important for countries in South Asia and East Africa (Goddard and Graham, 1999; Black et al., 2003), while the East African highlands are one of the topographies forcing climate change over the West Indian Ocean (Slingo et al., 2005). Here, we show the influences of the East African highlands by comparing experiments between amip r1i1p1f1 and amip-hld r1i1p1f1 in Fig. 7. Figure 7a shows the JJA differences of the precipitation and 850-hPa winds. A strong anticyclonic anomaly appears over the North Arabian Sea, leading to a strong easterly along the East coast of the tropical African continent. The precipita-

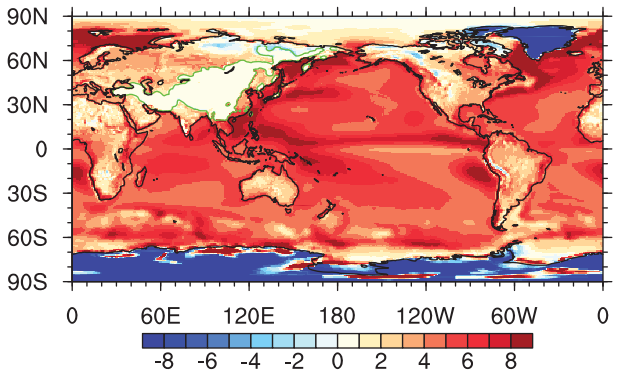

Fig. 5. Climatological mean (1979–2014) of vertical diffusion heating (shaded; units: K d^{-1}) at the surface in amip-TIP-nosh. The thick black contour denotes the 500-m topographic height. The green contour denotes the region where the vertical diffusion heating is modified.

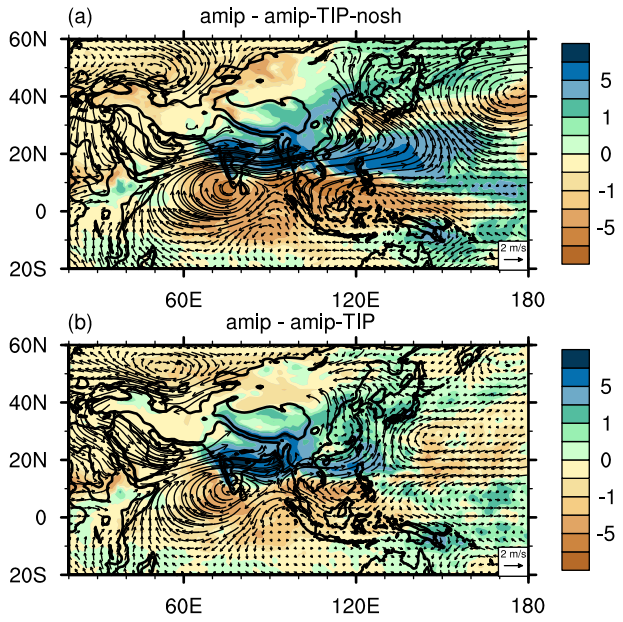

Fig. 6. Climatological (1979–2014) JJA mean precipitation (shaded; units: mm d^{-1}) and 850-hPa wind (vectors; units: m s^{-1}) differences between (a) amip r1i1p1f1 and amip-TIP-nosh r1i1p1f1, and (b) amip r1i1p1f1 and amip-TIP r1i1p1f1. The thick black contour denotes the 500- and 3000-m topographic heights, respectively.

tion anomaly shows a dipole pattern over the West Indian Ocean with decreases in the Arabian Sea and Bay of Bengal but an increase in the tropical central Indian Ocean. The precipitation over central Africa is also increased. The spatial patterns of precipitation and winds are similar to those in Fig. 7f and Fig. 8f of Slingo et al. (2005), who studied the influence of the East African Highlands by the Hadley Centre's climate model (HadAM3). For December–January–February (DJF) (Fig. 7b), the East African Highlands induce cyclonic circulation over Northeast Africa and the Arabian Peninsula, accompanied by increased precipitation on the east of the cyclonic anomaly. In the Southern Hemisphere, the topographic forcing induces a northerly wind along the east coast of Africa, increased precipitation over the West Indian Ocean, and decreased precipitation over the East Indian Ocean, which are roughly similar to Figs. 7c and 8c in Slingo et al. (2005).

The Sierra Madre Mountains are important to the formation of the North American monsoon system (Adams and Comrie, 1997) and to the East Pacific typhoon activities (Zehnder, 1993). We show the JJA differences of precipitation and 850-hPa winds between amip r1i1p1f1 and amip-hld r1i1p1f2 in Fig. 8a. The orographic forcing of the Sierra Madres clearly generates a low-level cyclonic circulation anomaly and leads to increased local precipitation. This pattern is reasonable according to the thermal adaption theory proposed by Wu and Liu. (2000), which states that the

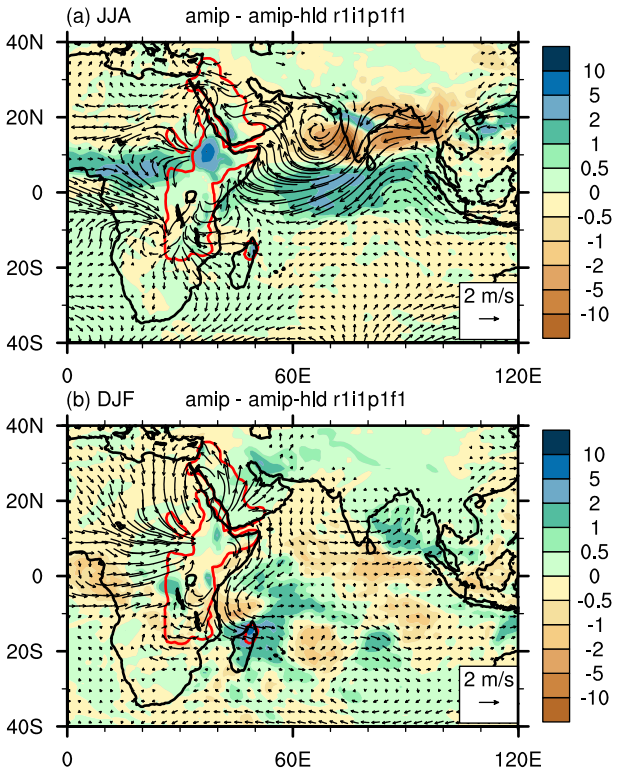

Fig. 7. (a) Climatological (1979–2014) JJA mean precipitation (shaded; units: mm d^{-1}) and 850-hPa wind (vectors; units: m s^{-1}) differences between amip r1i1p1f1 and amip-hld r1i1p1f1. (b) As in (a) but for the DJF mean. The red contour denotes the topography modified in amip-hld r1i1p1f1.

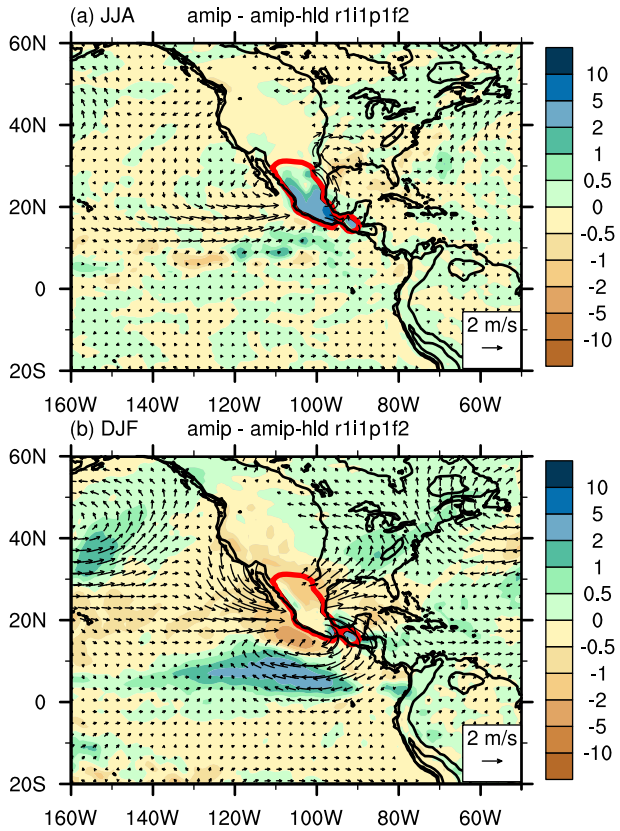

Fig. 8. (a) Climatological (1979–2014) JJA mean precipitation (shaded; units: mm d^{-1}) and 850-hPa wind (vectors; units: m s^{-1}) differences between amip r1i1p1f1 and amip-hld r1i1p1f2. (b) As in (a) but for the DJF mean. The red contour denotes the topography modified in amip-hld r1i1p1f2.

orography acts as a heating forcing in the lower troposphere during the summertime. For DJF (Fig. 8b), the Sierra Madre induces a cyclonic circulation anomaly to its north and an anticyclonic circulation anomaly to its south, accompanied by a decreased precipitation anomaly surrounding the mountains and an increased precipitation anomaly mainly over the East Pacific and the eastern part of the North American continent.

The Andes Mountains are the dominant topographic feature in South America. Previous literature suggests that the Andes are critical to the formation of the South American low-level jet (Gandu and Geisler, 1991; Campetella and Vera, 2002), moisture transport, convection, and precipitation over South America (Insel et al., 2010; Junquas et al., 2016). In our experiments, we remove the Andes Mountains in amip-hld r1i1p1f3. The differences between amip r1i1p1f1 and amip-hld r1i1p1f3 are shown in Fig. 9. The JJA difference of the 850-hPa circulation (Fig. 9a) shows a cyclonic anomaly over subtropical South America and a strong westerly anomaly over the eastern tropical Pacific, accompanied by increased precipitation over the East Pacific around 10°N and along the meridionally oriented Andes. For DJF (Fig. 9b), the difference in the wind anomaly is quite close to the JJA pattern, while the difference in the precipitation anomaly shows an increase mainly over the south-

ern part of South America and a decrease over the Amazon Basin, which is close to Fig. 4 in Junquas et al. (2016).

Based on the above analysis, the basic performance of the CAS FGOALS-f3-L model in the GMMIP Tier-1 & Tier-3 experiments is justified. Finally, we show some more information on the output datasets. The output contains high temporal frequency (three-hourly mean, six-hourly snapshot and mean) datasets for the amip-TIP and amip-TIP-nosh experiments, which is beyond the requirement of GMMIP. The total size of the amip-TIP and amip-TIP-nosh experiments is approximately 2.5 TB each, and the total sizes of amip-hld r1i1p1f1, amip-hld r1i1p1f2 and amip-hld r1i1p1f3 are approximately 0.3 TB each. Detailed information on the output variables is also shown in Table 2 for reference.

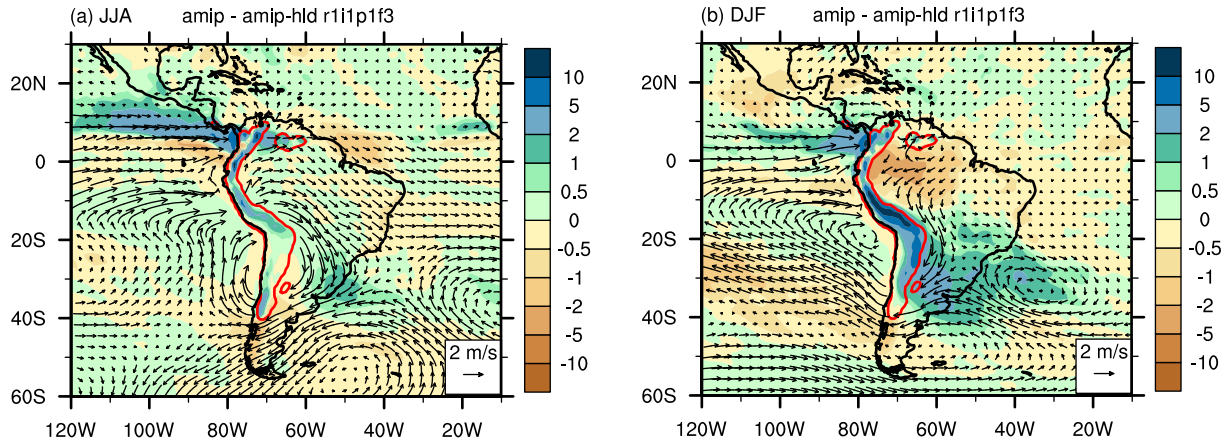

Fig. 9. (a) Climatological (1979–2014) JJA mean precipitation (shaded; units: mm d^{-1}) and 850-hPa wind (vectors; units: m s^{-1}) differences between amip r1i1p1f1 and amip-hld r1i1p1f3. (b) As in (a) but for the DJF mean. The red contour denotes the topography modified in amip-hld r1i1p1f3.

Table 2. CAS FGOALS-f3-L output variables prepared for CMIP6 GMMIP experiments.

Output name	Description	Frequency (3-h mean, 6-h snapshot only for amip-TIP and amip-TIP-nosh)
rlut	TOA outgoing longwave radiation	Monthly
rsdt	TOA incident shortwave radiation	Monthly
rsut	TOA outgoing shortwave radiation	Monthly
rlutcs	TOA outgoing clear-sky longwave radiation	Monthly
rsutcs	TOA outgoing clear-sky shortwave radiation	Monthly
rlds	Surface downwelling longwave radiation	Monthly, 3 h
rlus	Surface upwelling longwave radiation	Monthly, 3 h
rsds	Surface downwelling shortwave radiation	Monthly, 3 h
rsus	Surface upwelling shortwave radiation	Monthly, 3 h
rldscs	Surface downwelling clear-sky longwave radiation	Monthly, 3 h
rsdscs	Surface downwelling clear-sky shortwave radiation	Monthly, 3 h
rsuscs	Surface upwelling clear-sky shortwave radiation	Monthly, 3 h
tauu	Surface downward eastward wind stress	Monthly
tauv	Surface downward northward wind stress	Monthly
hfss	Surface upward sensible heat flux	Monthly, 3 h
hfls	Surface upward latent heat flux	Monthly, 3 h
pr	Precipitation	Monthly, daily, 3 h
evspsbl	Evaporation	Monthly
ts	Surface skin temperature	Monthly
tas	Near-surface air temperature	Monthly, daily, 3 h
tasmax	Daily maximum near-surface air temperature	Monthly, daily
tasmin	Daily minimum near-surface air temperature	Monthly, daily
uas	Eastward near-surface wind	Monthly, 3 h
vas	Northward near-surface wind	Monthly, 3 h
sfcWind	Near-surface wind speed	Monthly
huss	Near-surface specific humidity	Monthly, daily, 3 h

Table 2. (Continued)

Output name	Description	Frequency (3-h mean, 6-h snapshot only for amip-TIP and amip-TIP-nosh)
hurs	Near-surface relative humidity	Monthly, daily
clt	Total cloud fraction	Monthly, 3 h
ps	Surface air pressure	Monthly, 3 h, 6 h
psl	Sea level pressure	Monthly, daily
snc	Snow area fraction	Monthly, 3 h
ta	Air temperature at model level	Monthly, 6 h
ua	Eastward wind at model level	Monthly, 6 h
va	Northward wind at model level	Monthly, 6 h
hus	Specific humidity at model level	Monthly, 6 h
hur	Relative humidity at model level	Monthly
zg	Geopotential height at model level	Monthly

Acknowledgements. The research presented in this paper was funded by the National Natural Science Foundation of China (Grant Nos. 91737306, 91637312, 41730963, 91837101, 91637208, 41530426), and the Key Research Program of Frontier Sciences, Chinese Academy of Sciences (Grant QYZDY-SSW-DQC018).

Data availability statement

The data that support the findings of this study are available from the following open sources: https://esgf-node.llnl.gov/projects/cmip6/.

Disclosure statement

No potential conflicts of interest are reported by the authors.

REFERENCES

Abe, M., A. Kitoh, and T. Yasunari, 2003: An evolution of the Asian summer monsoon associated with mountain uplift–Simulation with the MRI atmosphere-ocean coupled GCM. *J. Meteor. Soc. Japan*, **81**(5), 909–933, https://doi.org/10.2151/jmsj.81.909.

Adams, D. K., and A. C. Comrie, 1997: The North American monsoon. *Bull. Amer. Meteor. Soc.*, **78**(10), 2197–2214, https://doi.org/10.1175/1520-0477(1997)078<2197:TNAM>2.0.CO;2.

Bao, Q., and Coauthors, 2013: The flexible global ocean-atmosphere-land system model, spectral version 2: FGOALS-s2. *Adv. Atmos. Sci.*, **30**(3), 561–576, https://doi.org/10.1007/s00376-012-2113-9.

Bao, Q., G. X. Wu, Y. M. Liu, J. Yang, Z. Z. Wang, and T. J. Zhou, 2010: An introduction to the coupled model FGOALS1.1-s and its performance in East Asia. *Adv. Atmos. Sci.*, **27**(5), 1131–1142, https://doi.org/10.1007/s00376-010-9177-1.

Bao, Q., X. F. Wu, J. X. Li, L. Wang, B. He, X. C. Wang, Y. M. Liu, and G. X. Wu, 2019: Outlook for El Niño and the Indian Ocean Dipole in autumn-winter 2018–2019. *Chinese Science Bulletin*, **64**, 73–78, https://doi.org/10.1360/N972018-00913.

Becker, A., P. Finger, A. Meyer-Christoffer, B. Rudolf, K. Schamm, U. Schneider, and M. Ziese, 2013: A description of the global land-surface precipitation data products of the Global Precipitation Climatology Centre with sample applications including centennial (trend) analysis from 1901-present. *Earth System Science Data*, **5**, 71–99, https://doi.org/10.5194/essd-5-71-2013.

Black, E., J. Slingo, and K. R. Sperber, 2003: An observational study of the relationship between excessively strong short rains in coastal East Africa and Indian Ocean SST. *Mon. Wea. Rev.*, **131**, 74–94, https://doi.org/10.1175/1520-0493(2003)131<0074:AOSOTR>2.0.CO;2.

Boos, W. R., and Z. M. Kuang, 2010: Dominant control of the South Asian monsoon by orographic insulation versus plateau heating. *Nature*, **463**(7278), 218–222, https://doi.org/10.1038/nature08707.

Boos, W. R., and Z. M. Kuang, 2013: Sensitivity of the South Asian monsoon to elevated and non-elevated heating. *Scientific Reports*, **3**, 1192, https://doi.org/10.1038/srep01192.

Bretherton, C. S., and S. Park, 2009: A new moist turbulence parameterization in the community atmosphere model. *J. Climate*, **22**(12), 3422–3448, https://doi.org/10.1175/2008JCLI2556.1.

Campetella, C. M., and C. S. Vera, 2002: The influence of the Andes Mountains on the South American low-level flow. *Geophys. Res. Lett.*, **29**(17), 1826, https://doi.org/10.1029/2002GL015451.

Cook, K. H., G. A. Meehl, and J. M. Arblaster, 2012: Monsoon regimes and processes in CCSM4. Part II: African and American monsoon systems. *J. Climate*, **25**, 2609–2621, https://doi.org/10.1175/JCLI-D-11-00185.1.

Enfield, D. B., A. M. Mestas-Nuñez, and P. J. Trimble, 2001: The Atlantic Multidecadal Oscillation and its relation to rainfall and river flows in the continental U. *S. Geophys. Res. Lett.*, **28**, 2077–2080, https://doi.org/10.1029/2000GL012745.

Folland, C. K., T. N. Palmer, and D. E. Parker, 1986: Sahel rainfall and worldwide sea temperatures, 1901–85. *Nature*, **320**, 602–607, https://doi.org/10.1038/320602a0.

Gandu, A. W., and J. E. Geisler, 1991: A primitive equations model study of the effect of topography on the summer circula-

tion over tropical South America. *J. Atmos. Sci.*, **48**, 1822–1836, https://doi.org/10.1175/1520-0469(1991)048<1822:APEMSO>2.0.CO;2.

Goddard, L., and N. E. Graham, 1999: Importance of the Indian Ocean for simulating rainfall anomalies over eastern and southern Africa. *J. Geophys. Res.*, **104**, 19 099–19 116, https://doi.org/10.1029/1999JD900326.

Goswami, B. N., M. S. Madhusoodanan, C. P. Neema, and D. Sengupta, 2006: A physical mechanism for North Atlantic SST influence on the Indian summer monsoon. *Geophys. Res. Lett.*, **33**, L02706, https://doi.org/10.1029/2005GL024803.

Hahn, D. G., and S. Manabe, 1975: The role of mountains in the south Asian monsoon circulation. *J. Atmos. Sci.*, **32**(8), 1515–1541, https://doi.org/10.1175/1520-0469(1975)032<1515:TROMIT>2.0.CO;2.

Hansen, J. R., R. Ruedy, M. Sato, K. Lo, 2010: Global surface temperature change. *Rev. Geophys.*, **48**, RG4004.

Harris, L. M., and S.-J. Lin, 2014: Global-to-regional nested grid climate simulations in the GFDL high resolution atmospheric model. *J. Climate*, **27**(13), 4890–4910, https://doi.org/10.1175/JCLI-D-13-00596.1.

He, B., G. X. Wu, Y. M. Liu, and Q. Bao, 2015: Astronomical and hydrological perspective of mountain impacts on the Asian summer monsoon. *Scientific Reports*, **5**, 17586, https://doi.org/10.1038/srep17586.

He, B., and Coauthors, 2019: CAS FGOALS-f3-L model datasets for CMIP6 historical atmospheric model intercomparison project simulation. *Adv. Atmos. Sci.*, **36**(8), 771–778, https://doi.org/10.1007/s00376-019-9027-8.

Hunke, E. C., W. H. Lipscomb, A. K. Turner, N. Jeffery, and S. Elliott, 2010: CICE: The los alamos sea ice model documentation and software user's manual version 4.1. LA-CC-06-012, 675 pp.

Hurtt, G. C., and Coauthors, 2009: Harmonisation of global land-use scenarios for the period 1500–2100 for IPCC-AR5. iLEAPS Newsletter, No.7, 6–8.

Insel, N., C. J. Poulsen, and T. A. Ehlers, 2010: Influence of the Andes Mountains on South American moisture transport, convection, and precipitation. *Climate Dyn.*, **35**(7–8), 1477–1492, https://doi.org/10.1007/s00382-009-0637-1.

Junquas, C., L. Li, C. S. Vera, H. Le Treut, and K. Takahashi, 2016: Influence of South America orography on summertime precipitation in southeastern South America. *Climate Dyn.*, **46**(11–12), 3941–3963, https://doi.org/10.1007/s00382-015-2814-8.

Kitoh, A., 1997: Mountain uplift and surface temperature changes. *Geophys. Res. Lett.*, **24**(2), 185–188, https://doi.org/10.1029/96GL03953.

Kitoh, A., H. Endo, K. K. Kumar, I. F. A. Cavalcanti, P. Goswami, and T. J. Zhou, 2013: Monsoons in a changing world: A regional perspective in a global context. *J. Geophys. Res.*, **118**, 3053–3065, https://doi.org/10.1002/jgrd.50258.

Lamarque, J. F., and Coauthors, 2012: CAM-chem: Description and evaluation of interactive atmospheric chemistry in the community earth system model. *Geoscientific Model Development*, **5**(2), 369–411, https://doi.org/10.5194/gmd-5-369-2012.

Li, J. X., Q. Bao, Y. M. Liu, G. X. Wu, L. Wang, B. He, X. C. Wang, J. D. Li, 2019: Evaluation of FAMIL2 in simulating the climatology and seasonal-to-interannual variability of tropical cyclone characteristics. *Journal of Advances in Modeling Earth Systems*, **11**(4), 1117–1136, https://doi.org/10.1029/2018MS001506.

Lin, S. J., 2004: A "vertically Lagrangian" finite-volume dynamical core for global models. *Mon. Wea. Rev.*, **132**(10), 2293–2307, https://doi.org/10.1175/1520-0493(2004)132<2293:AVLFDC>2.0.CO;2.

Lin, Y. L., R. D. Farley, and H. D. Orville, 1983: Bulk parameterization of the snow field in a cloud model. *J. Climate Appl. Meteor.*, **22**(6), 1065–1092, https://doi.org/10.1175/1520-0450(1983)022<1065:BPOTSF>2.0.CO;2.

Liu, H. L., P. F. Lin, Y. Q. Yu, and X. H. Zhang, 2012: The baseline evaluation of LASG/IAP climate system ocean model (LICOM) version 2. *Acta Meteorologica Sinica*, **26**(3), 318–329, https://doi.org/10.1007/s13351-012-0305-y.

Liu, Y. M., B. J. Hoskins, and M. Blackburn, 2007: Impact of Tibetan orography and heating on the summer flow over Asia. *J. Meteor. Soc. Japan*, **85B**, 1–19, https://doi.org/10.2151/jmsj.85B.1.

Lu, R. Y., B. W. Dong, and H. Ding, 2006: Impact of the Atlantic Multidecadal Oscillation on the Asian summer monsoon. *Geophys. Res. Lett.*, **33**, L24701, https://doi.org/10.1029/2006GL027655.

Mantua, N. J., and S. R. Hare, 2002: The pacific decadal oscillation. *J. Oceanogr.*, **58**, 35–44, https://doi.org/10.1023/A:1015820616384.

Matthes, K., and Coauthors, 2017: Solar forcing for CMIP6 (v3.2). *Geoscientific Model Development*, **10**, 2247–2302, https://doi.org/10.5194/gmd-10-2247-2017.

Meinshausen, M., and Coauthors, 2017: Historical greenhouse gas concentrations for climate modelling (CMIP6). *Geoscientific Model Development*, **10**, 2057–2116, https://doi.org/10.5194/gmd-10-2057-2017.

Okajima, H., and S. P. Xie, 2007: Orographic effects on the northwestern Pacific monsoon: Role of air-sea interaction. *Geophys. Res. Lett.*, **34**(21), L21708, https://doi.org/10.1029/2007GL032206.

Oleson, K. W., and Coauthors, 2010: Technical description of version 4.0 of the Community Land Model (CLM). NCAR Technical Note NCAR/TN-478+STR, 173 pp.

Palmer, T. N., G. J. Shutts, and R. Swinbank, 1986: Alleviation of a systematic westerly bias in general circulation and numerical weather prediction models through an orographic gravity wave drag parametrization. *Quart. J. Roy. Meteor. Soc.*, **112**(474), 1001–1039, https://doi.org/10.1002/qj.49711247406.

Power, S., T. Casey, C. Folland, A. Colman, and V. Mehta, 1999: Inter-decadal modulation of the impact of ENSO on Australia. *Climate Dyn.*, **15**, 319–324, https://doi.org/10.1007/s003820050284.

Putman, W. M., and S. J. Lin, 2007: Finite-volume transport on various cubed-sphere grids. *J. Comput. Phys.*, **227**(1), 55–78, https://doi.org/10.1016/j.jcp.2007.07.022.

Queney, P., 1948: The problem of air flow over mountains: A summary of theoretical studies. *Bull. Amer. Meteor. Soc.*, **29**(1), 16–26, https://doi.org/10.1175/1520-0477-29.1.16.

Slingo, J., H. Spencer, B. Hoskins, P. Berrisford, and E. Black, 2005: The meteorology of the Western Indian Ocean, and the influence of the East African Highlands. *Philosophical Transactions of the Royal Society A: Mathematical, Physical and Engineering Sciences*, **363**(1826), 25–42, https://doi.org/10.1098/rsta.2004.1473.

Song, F. H., and T. J. Zhou, 2014a: Interannual variability of East Asian summer monsoon simulated by CMIP3 and CMIP5

AGCMs: Skill dependence on Indian Ocean-western Pacific anticyclone teleconnection. *J. Climate*, **27**, 1679–1697, https://doi.org/10.1175/JCLI-D-13-00248.1.

Song, F. F., and T. J. Zhou, 2014b: The climatology and interannual variability of East Asian summer monsoon in CMIP5 coupled models: Does air-sea coupling improve the simulations? *J. Climate*, **27**, 8761–8777, https://doi.org/10.1175/JCLI-D-14-00396.1.

Sperber, K. R., H. Annamalai, I. S. Kang, A. Kitoh, A. Moise, A. Turner, B. Wang, and T. Zhou, 2013: The Asian summer monsoon: An intercomparison of CMIP5 vs. CMIP3 simulations of the late 20th century. *Climate Dyn.*, **41**, 2711–2744, https://doi.org/10.1007/s00382-012-1607-6.

Sutton, R. T., and D. L. R. Hodson, 2005: Atlantic ocean forcing of North American and European summer climate. *Science*, **309**, 115–118, https://doi.org/10.1126/science.1109496.

Wang, B., 1994: Climatic regimes of tropical convection and rainfall. *J. Climate*, **7**, 1109–1118, https://doi.org/10.1175/1520-0442(1994)007<1109:CROTCA>2.0.CO;2.

Wang, B., and Q. H. Ding, 2008: Global monsoon: Dominant mode of annual variation in the tropics. *Dyn. Atmos. Oceans*, **44**, 165–183, https://doi.org/10.1016/j.dynatmoce.2007.05.002.

Wang, B., Q. H. Ding, X. H. Fu, I. S. Kang, K. Jin, J. Shukla, and F. Doblas-Reyes, 2005: Fundamental challenge in simulation and prediction of summer monsoon rainfall. *Geophys. Res. Lett.*, **32**, L15711, https://doi.org/10.1029/2005GL022734.

Wang, B., J. Liu, H. J. Kim, P. J. Webster, and S. Y. Yim, 2012: Recent change of the global monsoon precipitation (1979–2008). *Climate Dyn.*, **39**, 1123–1135, https://doi.org/10.1007/s00382-011-1266-z.

Wang, X. C., and M. H. Zhang, 2014: Vertical velocity in shallow convection for different plume types. *Journal of Advances in Modeling Earth Systems*, **6**(2), 478–489, https://doi.org/10.1002/2014MS000318.

Wu, G. X., and Y. M. Liu, 2000: Thermal adaptation, overshooting, dispersion, and subtropical anticyclone part I: Thermal adaptation and overshooting. *Chinese Journal of Atmospheric Sciences*, **24**(4), 433–446, https://doi.org/10.3878/j.issn.1006-9895.2000.04.01. (in Chinese with English abstract)

Wu, G. X., H. Liu, Y. C. Zhao, and W. P. Li, 1996: A nine-layer atmospheric general circulation model and its performance. *Adv. Atmos. Sci.*, **13**(1), 1–18, https://doi.org/10.1007/BF02657024.

Wu, G. X., and Coauthors, 2007: The influence of mechanical and thermal forcing by the Tibetan Plateau on Asian climate. *Journal of Hydrometeorology*, **8**(4), 770–789, https://doi.org/10.1175/JHM609.1.

Wu, G. X., Y. M. Liu, B. He, Q. Bao, A. M. Duan, and F. F. Jin, 2012: Thermal controls on the Asian summer monsoon. *Scientific Reports*, **2**, 404, https://doi.org/10.1038/srep00404.

Wu, G. X., B. He, Y. M. Liu, Q. Bao, and R. C. Ren, 2015: Location and variation of the summertime upper-troposphere temperature maximum over South Asia. *Climate Dyn.*, **45**(9–10), 2757–2774, https://doi.org/10.1007/s00382-015-2506-4.

Xu, K. M., and D. A. Randall, 1996: A semiempirical cloudiness parameterization for use in climate models. *J. Atmos. Sci.*, **53**(21), 3084–3102, https://doi.org/10.1175/1520-0469(1996)053<3084:ASCPFU>2.0.CO;2.

Zehnder, J. A., 1993: The influence of large-scale topography on barotropic vortex motion. *J. Atmos. Sci.*, **50**(15), 2519–2532, https://doi.org/10.1175/1520-0469(1993)050<2519:TIOLST>2.0.CO;2.

Zhou, L. J., Y. M. Liu, Q. Bao, H. Y. Yu, G. X. Wu, 2012: Computational Performance of the High-Resolution Atmospheric Model FAMIL. *Atmospheric and Oceanic Science Letters*, **5**(5), 355–359, https://doi.org/10.1080/16742834.2012.11447024.

Zhou, L. J., and Coauthors, 2015: Global energy and water balance: Characteristics from Finite-volume Atmospheric Model of the IAP/LASG (FAMIL1). *Journal of Advances in Modeling Earth Systems*, **7**(1), 1–20, https://doi.org/10.1002/2014MS000349.

Zhou T. J., B. Wu, and B. Wang, 2009a: How well do atmospheric general circulation models capture the leading modes of the interannual variability of the Asian-Australian Monsoon? *J. Climate*, **22**, 1159–1173, https://doi.org/10.1175/2008JCLI2245.1.

Zhou, T. J., D. Gong, J. Li, and B. Li, 2009b: Detecting and understanding the multi-decadal variability of the East Asian Summer Monsoon–Recent progress and state of affairs. *Meteor. Z.*, **18**, 455–467, https://doi.org/10.1127/0941-2948/2009/0396.

Zhou, T. J., and Coauthors, 2016: GMMIP (v1.0) contribution to CMIP6: Global monsoons model inter-comparison project. *Geoscientific Model Development*, **9**(10), 3589–3604, https://doi.org/10.5194/gmd-9-3589-2016.

Zhou, X. J., P. Zhao, J. M. Chen, L. X. Chen, and W. L. Li, 2009c: Impacts of thermodynamic processes over the Tibetan Plateau on the Northern Hemispheric climate. *Science in China Series D: Earth Sciences*, **52**(11), 1679–1693, https://doi.org/10.1007/s11430-009-0194-9.